

See discussions, stats, and author profiles for this publication at: <https://www.researchgate.net/publication/271714459>

Interface Engineering of Perovskite Hybrid Solar Cells with Solution-Processed Perylene-Diimide Heterojunctions toward High Performance

ARTICLE in CHEMISTRY OF MATERIALS · JANUARY 2015

Impact Factor: 8.35 · DOI: 10.1021/cm5037919

CITATIONS

25

READS

252

13 AUTHORS, INCLUDING:



Jie Min

Institute Materials for Electronics and Energy ...

46 PUBLICATIONS 1,156 CITATIONS

[SEE PROFILE](#)



Fei Guo

Friedrich-Alexander-University of Erlangen-Nü...

15 PUBLICATIONS 162 CITATIONS

[SEE PROFILE](#)



Hamed Azimi

Friedrich-Alexander-University of Erlangen-Nü...

30 PUBLICATIONS 826 CITATIONS

[SEE PROFILE](#)



Tayebeh Ameri

Friedrich-Alexander-University of Erlangen-Nü...

72 PUBLICATIONS 2,140 CITATIONS

[SEE PROFILE](#)

Interface Engineering of Perovskite Hybrid Solar Cells with Solution-Processed Perylene–Diimide Heterojunctions toward High Performance

Jie Min,[†] Zhi-Guo Zhang,^{*,‡} Yi Hou,^{†,§} Cesar Omar Ramirez Quiroz,[†] Thomas Przybilla,^{||} Carina Bronnbauer,^{†,§} Fei Guo,[†] Karen Forberich,[†] Hamed Azimi,^{*,†} Tayebeh Ameri,[†] Erdmann Spiecker,^{||} Yongfang Li,[†] and Christoph J. Brabec^{†,⊥}

[†]Institute of Materials for Electronics and Energy Technology (I-MEET), Friedrich-Alexander-University Erlangen-Nuremberg, Martensstraße 7, 91058 Erlangen, Germany

[‡]CAS Key Laboratory of Organic Solids, Institute of Chemistry, Chinese Academy of Sciences, Beijing 100190, China

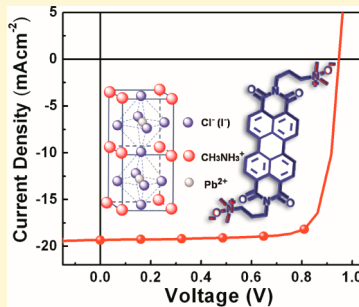
[§]Erlangen Graduate School in Advanced Optical Technologies (SAOT), Paul-Gordan-Str. 6, 91052 Erlangen, Germany

^{||}Center for Nanoanalysis and Electron Microscopy, Friedrich-Alexander-Universität Erlangen-Nürnberg, Cauerstraße 6, 91058 Erlangen, Germany

[⊥]Bavarian Center for Applied Energy Research (ZAE Bayern), Haberstraße 2a, 91058 Erlangen, Germany

S Supporting Information

ABSTRACT: Perovskite hybrid solar cells (pero-HSCs) were demonstrated to be among the most promising candidates within the emerging photovoltaic materials with respect to their power conversion efficiency (PCE) and inexpensive fabrication. Further PCE enhancement mainly relies on minimizing the interface losses via interface engineering and the quality of the perovskite film. Here, we demonstrate that the PCEs of pero-HSCs are significantly increased to 14.0% by incorporation of a solution-processed perylene–diimide (PDINO) as cathode interface layer between the [6,6]-phenyl-C61 butyric acid methyl ester (PCBM) layer and the top Ag electrode. Notably, for PDINO-based devices, prominent PCEs over 13% are achieved within a wide range of the PDINO thicknesses (5–24 nm). Without the PDINO layer, the best PCE of the reference PCBM/Ag device was only 10.0%. The PCBM/PDINO/Ag devices also outperformed the PCBM/ZnO/Ag devices (11.3%) with the well-established zinc oxide (ZnO) cathode interface layer. This enhanced performance is due to the formation of a highly qualitative contact between PDINO and the top Ag electrode, leading to reduced series resistance (R_s) and enhanced shunt resistance (R_{sh}) values. This study opens the door for the integration of a new class of easily-accessible, solution-processed high-performance interfacial materials for pero-HSCs.



1. INTRODUCTION

Hybrid solar cells (HSCs) using organometal halide perovskites as light absorbers have been intensively studied in the recent 4 years as a next-generation photovoltaic technology that can address the scalability changes in combination with low-cost solution processing.^{1–5} Organolead halide perovskite materials, ABX_3 (A = CH_3NH_3 or NHCHNH_3 , B = Pb, and X = Br, Cl, or I), are the subject of extensive investigations. This kind of perovskite absorbers possess several attractive features including broad light absorption from the visible to the near-infrared region, a high extinction coefficient, large charge carrier diffusion lengths, low-temperature solution-processability, and tunable optical and electronic properties via compositional changes.^{1,6–8} Recently, perovskite-based HSCs (pero-HSCs) from the $\text{CH}_3\text{NH}_3\text{PbI}_{3-x}\text{Cl}_x$ sensitizer family have reached power conversion efficiencies (PCEs) of >15%,^{5,11} for both device architectures of a mesoscopic bulk heterojunction^{1,9} and a planar heterojunction one.¹⁰ These attract tremendous attention in the photovoltaic industry. Efficiencies exceeding

20% might be realized by further optimization of the perovskite film quality and the interface engineering, or by introducing tandem architectures with multiple-junction solar cells.^{3,12}

Normally, pero-HSC architectures can be classified according to their heterojunction sequence as a conventional (compact TiO_2 (n)/Perovskite (i)/organic semiconductors (p))^{10,13,14} or inverted (poly(3,4-ethylenedioxythiophene):polystyrene sulfonic acid (PEDOT:PSS) (p) /Perovskite (i) /fullerene derivatives (n))^{15–17} structure. In these heterojunctions, the main challenges encountered in perovskite devices are the control of the perovskite crystallization process and the interface engineering preventing recombination defects between the different interface layers. On the one hand, a poor perovskite film morphology has been cited as very detrimental to the device performance.^{13,14,18} On the other hand, since this

Received: October 15, 2014

Revised: December 1, 2014

Published: December 8, 2014



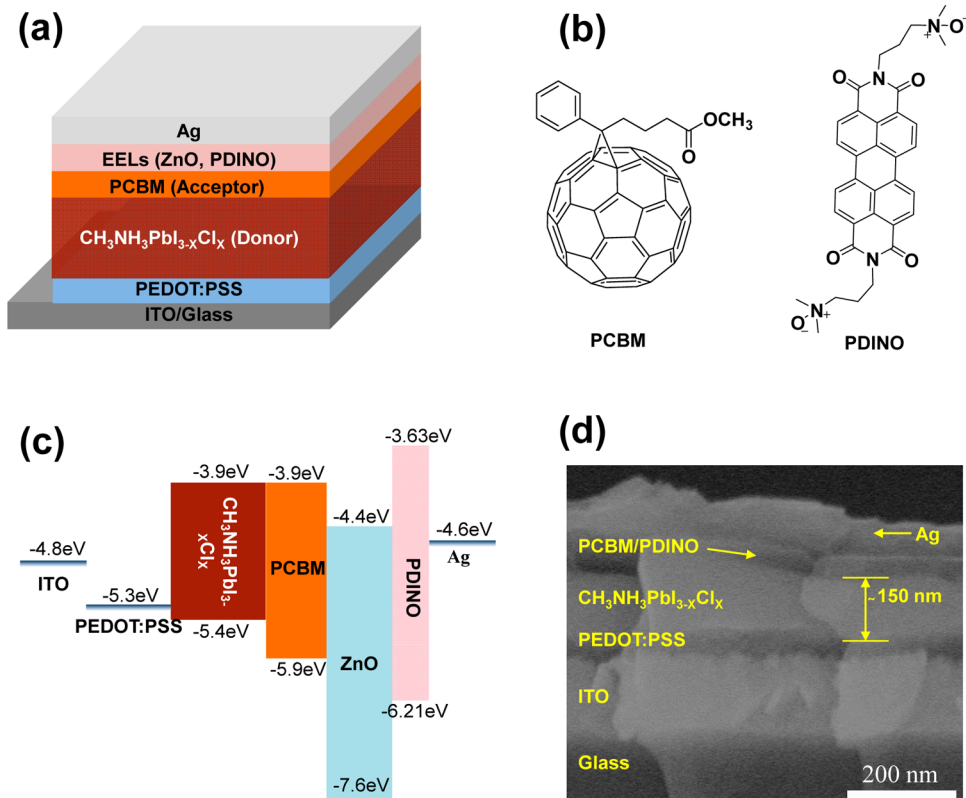


Figure 1. (a) Device structure of the p-i-n pero-HSCs. (b) Molecular structures of the PCBM and PDINO used for device fabrication. (c) Schematic representation of the band energy diagrams for the p-i-n configuration of pero-HSCs. (d) SEM cross-sectional image of the pero-HSC using PDINO as an EEL.

class of perovskites possesses long exciton diffusion lengths (100–1000 nm) and lifetimes (~100 ns) as compared with the rather short exciton diffusion lengths (~10 nm) and lifetimes (~10 ns) of organic semiconductors caused by tightly bounded electron–hole pairs,^{13,15,19} pero-HSC will be more prone to surface recombination due to imperfect crystal passivation and undesirable interfacial properties, resulting in fill factor (FF) and short-circuit current (J_{sc}) losses.^{20,21} More recently, effects on the controlling of the perovskite crystallization process and the interface engineering preventing recombination losses have boosted device efficiencies increased remarkably with an n-i-p heterojunction, and notably lead a record-breaking efficiency of 19.3% by Yang et al.²²

Despite its great success, the fabrication of most efficient perovskite solar cells is generally performed based on employing high-quality condensed compact metal oxide layers (such as TiO₂), which is needed sintered by a high temperature over 400 °C for a long time (1 h).^{21,23,24} This high-temperature device fabrication results in their high cost production, renders this technology incompatible with plastic substrates, and prevents its use in multijunction device architectures. As an alternative approach, efficient perovskite solar cells can be also fabricated with a planar p-i-n heterojunction as mentioned above, in which the perovskite layer is sandwiched between a hole-transport layer, PEDOT:PSS, and an electron-transport layer, [6,6]-phenyl-C₆₁-butyricacid methyl (PCBM). Without using the sintered compact metal oxide layers, this planar architecture potentially provides enhanced simplicity, flexibility, and low-temperature solution-processability for device optimization and multijunction construction.^{17,21,25} However, the alternative approach has not yet achieved comparable device

performance with the conventional high-temperature process. One associated reason is with the energy offset between a Fermi level of high work function metals (such as Ag and Au) and the lowest unoccupied molecular orbital (LUMO) of the organic material (PCBM).^{26–28} As demonstrated in organic photovoltaics, the existence of an energy barrier would significantly influence built-in potential and charge carrier extraction.²⁸ Moreover, compared with organic photovoltaics, pero-HSC will be more prone to surface recombination resulting from imperfect crystal passivation and undesirable interfacial properties.²⁰

Therefore, it is necessary to pay significantly more attention to engineering customized interfaces for pero-HSCs with a conventional architecture. This leads to effects on interfacial engineering in organic/inorganic planar pero-HSCs to passivate the defects at both the perovskite surface and the grain boundaries. Thus, thermal vapor deposited LiF,²⁹ Ca,³⁰ bathocuproine (BCP),^{17a,21} or fullerene (C₆₀)^{17a} on top of the PCBM layer are carried out, and a prominent device with high FF was realized. Although new device structures were introduced for improving the resistance of the fullerene layer, significant problems remained in terms of reduced device efficiency or the need for high-vacuum processing to deposit the composite layer as cathode.^{17,31} It is worth to mention that Snaith et al. developed highly efficient pero-HSCs by depositing an n-type TiO_x layer between the PCBM/Al interface via low-temperature solution-processing.^{16a} In addition, the Bis-C₆₀ surfactant^{15a} and amino-functionalized polymer (PN4N)^{15b} were also employed as an efficient electron-selective interfacial layer to align the energy levels between the perovskite semiconductor and top metal contact. These works highlighted

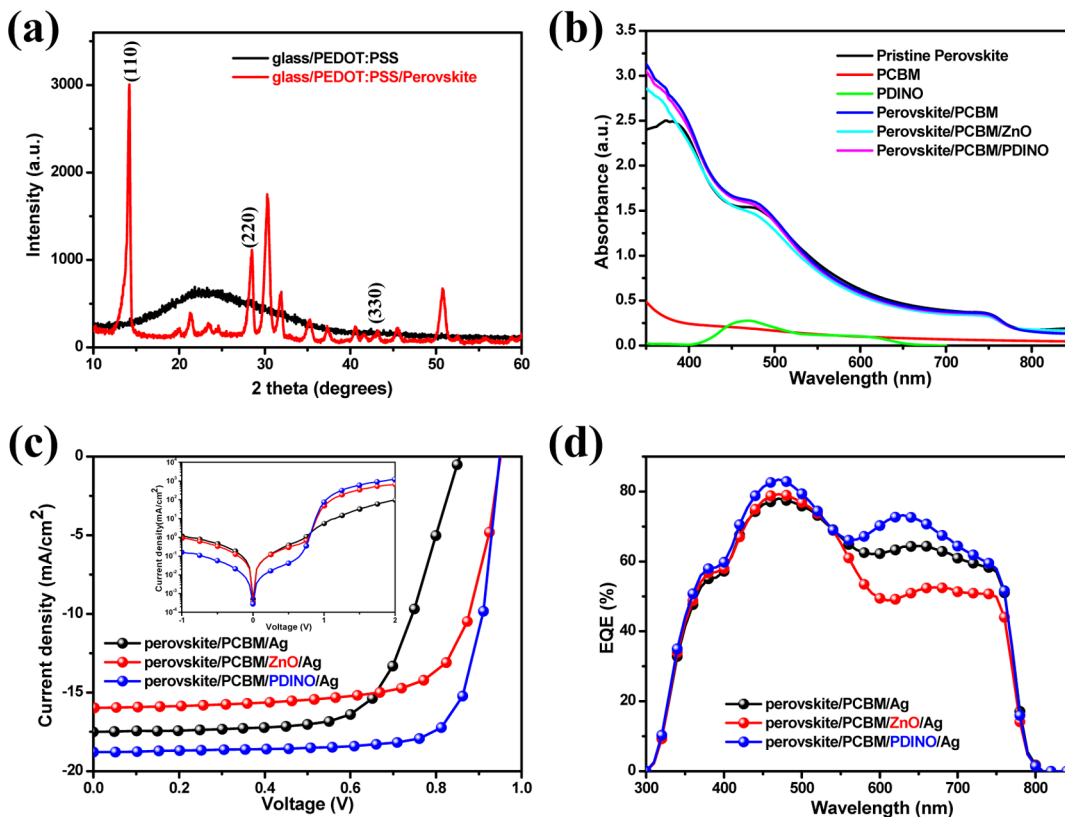


Figure 2. (a) XRD patterns of the glass/PEDOT:PSS and glass/PEDOT:PSS/perovskite samples. (b) UV-vis absorption spectra of PCBM, PDINO, and various perovskite-based composite films. (c) The current density–voltage (J – V) characteristics of the perovskite solar cells made from Ag, ZnO/Ag, and PDINO/Ag cathodes measured under illumination of an AM 1.5G solar simulator (100 mW cm^{-2}) in air. (d) EQE spectra of the pero-HSCs with different cathodes measured in air.

the direction of developing solution-processed cathode interlayers for pero-HSCs, allowing one to optimize the device performance as well as its stability.

Herein, we expanded the present rather limited range of the available electron extraction layer (EEL) for pero-HSCs and explored the perylene-diimide derivative (PDINO) as an effective EEL between PCBM and the top Ag electrode. Specially, different from other EELs that work well only at a critical ultrathin thickness due to its low conductivities, PDINO is a thickness-insensitive one that benefitted from its high conductivity. This intriguing feature renders it more suitable for inorganic photovoltaic films with a large boundary and rough surface, such as perovskite film, to realize conformal covering and eliminate the contact leakage. As a result, high efficiency pero-HSCs with a $V_{oc} = 0.95 \text{ V}$, a $J_{sc} = 18.8 \text{ mA/cm}^2$, and an FF of 78.5%, corresponding to a PCE of 14.0% measured in air under one sun illumination, was realized. This efficiency has significantly outperformed the control PCBM/Ag device (10.0%) without the PDINO layer and the PCBM/ZnO/Ag device (11.3%) with the ZnO layer used as the EEL layer for optimizing the contact properties of the PCBM/Ag interface. This study opens the door for utilizing a new class of easily accessible, solution-processed, perylene-diimide cathode interface layers to further improve the photovoltaic performance of pero-HSCs and other thin film solution processed solar cells.

2. RESULTS AND DISCUSSION

2.1. Device Fabrication and Characterization. A typical p-i-n pero-HSC structure is shown in Figure 1a, with the configuration of ITO/PEDOT:PSS/ $\text{CH}_3\text{NH}_3\text{PbI}_{3-x}\text{Cl}_x$ /

PCBM/EELs/Ag. Contrary to inverted pero-HSCs (n-i-p), which rely on *n*-type electron extraction layers as substrates, we employed a PEDOT:PSS layer, which is extensively used as a hole-transport layer in organic solar cells,^{32,33} deposited on top of glass/ITO anodes. The active layer of the pero-HSC is a planar heterojunction consisting of $\text{CH}_3\text{NH}_3\text{PbI}_{3-x}\text{Cl}_x$ and PCBM. Because of the long-range charge-carrier diffusion lengths (100–1000 nm) and lifetimes (~100 ns) inherent to the $\text{CH}_3\text{NH}_3\text{PbI}_{3-x}\text{Cl}_x$ perovskite,^{13,34} direct charge generation dominates the $\text{CH}_3\text{NH}_3\text{PbI}_{3-x}\text{Cl}_x$ perovskite bulk after absorption of light and these carriers are effectively separated at the donor/acceptor interface. In order to overcome the PCBM/Ag inherent losses, we introduced two different electron extraction layers (ZnO and PDINO) between PCBM and the Ag cathode. Parts (b) and (c) in Figure 1 show the corresponding molecular structures and the relative energy band diagram of the pero-HSCs, respectively. Here, the energy levels for the perovskite layer and PCBM were taken from the literature reported by Wen et al.³⁵ The energy levels for ZnO and PDINO were reported elsewhere.^{28,36} The LUMO level of PCBM is located in the vicinity of the top band edge of the perovskite layer, which is appropriate for retaining a high voltage in combination with reduced losses during the charge separation process. The lower energy offset between the LUMO (~3.63 eV) of PDINO and that of PCBM (~3.9 eV) should facilitate electron transfer from PCBM to PDINO and then to the top electrode. For the PDINO treated Ag electrode, the work function of Ag is lowered to 3.6 eV, thus providing larger built-in voltage across the device.³⁶ In addition, the highest occupied molecular orbital (HOMO) energy levels

Table 1. Photovoltaic Parameters of p-i-n pero-HSCs with Different Cathode Configurations^e

cathode configuration	V_{oc} [V]	J_{sc} [mA cm^{-2}]	J_{sc}^c [mA cm^{-2}]	FF [%]	PCE_{\max} ($\text{PCE}_{\text{ave}}^d$) [%]	R_s [$\Omega \text{ cm}^2$]	R_{sh} [$\text{k}\Omega \text{ cm}^2$]
PCBM/Ag	0.85	17.5	16.46	67.6	10.0 (9.8)	10.62	1.71
PCBM/ZnO/Ag ^a	0.95	16.0	14.95	74.5	11.3 (11.0)	1.35	2.28
PCBM/PDINO/Ag ^b	0.95	18.8	17.55	78.5	14.0 (13.7)	0.83	13.70

^aThe optimized thickness of ZnO layer is 40 nm. ^bThe thickness of PDINO layer is 15 nm, and the photovoltaic parameters of pero-HSCs with various PDINO thicknesses are shown in the Supporting Information. ^c J_{sc} values are calculated by EQE curves. ^dThe average PCE is obtained from six cells. The related photovoltaic parameters are shown in Figure S2 and Table S1 (Supporting Information). ^e The shunt resistance (R_{sh}) and series resistance (R_s) were calculated from the inverse of the slope of the $J-V$ curves at 0 and 2 V, respectively.

of ZnO and PDINO are estimated to be -7.6 and -6.21 eV, respectively, which are sufficiently low to efficiently block holes from the perovskite layer. The cross-sectional scanning electron microscope (SEM) image of the $\text{CH}_3\text{NH}_3\text{PbI}_{3-x}\text{Cl}_x$ perovskite device with PDINO as an EEL is presented in Figure 1d, showing a perovskite layer thickness of around 150 nm. The deposition of the PCBM/PDINO bilayer by spin-coating forms an \sim 60 nm capping layer. The cross-sectional SEM image of the PCBM/PDINO/Ag device showed that a well-defined layered planar structure was formed.

The crystalline structure of the $\text{CH}_3\text{NH}_3\text{PbI}_{3-x}\text{Cl}_x$ perovskite film on the glass/PEDOT:PSS substrate was characterized by the X-ray diffraction (XRD), as illustrated in Figure 2a. The glass/PEDOT:PSS substrate shows no characteristic peaks in the XRD pattern. In contrast, the X-ray diffractograms of the perovskite film on PEDOT:PSS coated glass substrates exhibited diffraction peaks at 14.18° , 28.51° , and 43.24° , assigned to the (110), (220), and (330) planes, respectively. Figure 2b shows the UV-vis spectrum of pristine PCBM, PDINO, and $\text{CH}_3\text{NH}_3\text{PbI}_{3-x}\text{Cl}_x$ perovskite on top of the PEDOT:PSS layer as well as their layer combinations. To investigate the effects of processing interface materials on top of the semiconductor, several identical $\text{CH}_3\text{NH}_3\text{PbI}_{3-x}\text{Cl}_x$ perovskite layers were coated with the various interface materials and were investigated by UV-vis spectroscopy. As shown in Figure 2b, the perovskite film showed an absorption onset at 800 nm together with a spectrally broad absorption feature ranging from the visible to the near-IR region, indicating the successful formation of $\text{CH}_3\text{NH}_3\text{PbI}_{3-x}\text{Cl}_x$ perovskite on a glass/PEDOT:PSS substrate. The perovskite/EEL multilayers showed the identical absorption as pristine $\text{CH}_3\text{NH}_3\text{PbI}_{3-x}\text{Cl}_x$ perovskite except in the range of 300–400 nm, where PCBM is strongly contributing. In addition, the almost unchanged absorption of perovskite/PCBM and perovskite/PCBM/PDINO films indicates that the deposition of PCBM and PDINO did not change the optical properties or the crystalline structure of the $\text{CH}_3\text{NH}_3\text{PbI}_{3-x}\text{Cl}_x$ perovskite film. Slight differences of the absorbance for the perovskite/PCBM/ZnO film may be caused by a different light propagation due to a rough ZnO film and not necessarily document a modification of the semiconductor layer.

2.2. Photovoltaic Properties. The $J-V$ characteristics of all the devices measured under illumination are shown in Figure 2c, and the photovoltaic performance of the pero-HSCs is summarized in Table 1. The control PCBM/Ag device exhibits a V_{oc} of 0.85 V, a J_{sc} of 17.5 mA cm^{-2} , an FF of 67.6%, a PCE of 10.0%, with a series resistance (R_s) of $10.62 \Omega \text{ cm}^2$ and a shunt resistance (R_{sh}) of $1.71 \text{ k}\Omega \text{ cm}^2$. The unfavorable contact between the PCBM/Ag interface results in a poorer diode characteristic and a lower FF value. After inserting the ZnO layer (40 nm), the PCBM/ZnO/Ag device shows a higher V_{oc} of 0.95 V, an increased FF of 74.5%, and a better PCE of 11.3%,

as illustrated in Table 1 and Figure 2c. The higher V_{oc} and FF values illustrate that the surface shunt between the PCBM/Ag interface was reduced. However, the PCBM/ZnO/Ag device exhibits a slightly lower J_{sc} as compared to the control device with a PCBM/Ag cathode, which, at first hand, seems to be inline with the absorption spectra (Figure 2b). A closer look to the external quantum efficiency (EQE) data (Figure 2d), however, reveals that, different from the absorption data, the photocurrent losses are spectrally pronounced only in the IR region. The reduced series resistance and the slightly enhanced shunt resistance suggest that ZnO reduces the electronic barrier between Ag and PCBM on the one hand, while reducing the Ag ion diffusion through the PCBM layer on the other hand. Although inserting a ZnO layer between the PCBM and the Ag cathode supports PCBM in forming a selective electron extraction contact with good V_{oc} and FF values, the slightly lower J_{sc} value indicates a related loss mechanism. Various scenarios may account for that. Because of the fairly good diode characteristics and the spectrally pronounced EQE changes, we exclude that processing of ZnO damages the perovskite layer. Most interestingly, a similar observation was recently reported for organic solar cells, where a nanoparticle charge extraction layer on top of an organic semiconductor layer gave reduced photocurrent densities. Stubhan et al. reported three possible loss mechanisms for this scenario.^{37a} One contribution arises from optical losses due to enhanced absorption in the interface layer as a result of a shifted interference pattern. A second contribution is R_s losses due to a rather low conductivity of the charge extraction layer. Finally, the third prominent influence on J_{sc} comes from significant particle agglomeration and increased surface roughness, leading to an inhomogeneous cathode layer and reduced current collection. Our current data on perovskite devices (see Table 1) exclude the second option (R_s losses). Previous optical simulations suggest that interference effects can cause changes in J_{sc} on the order of $\sim 1 \text{ mA cm}^{-2}$ as a function of the layer sequence and thickness.^{28,37} An optical simulation (see Figure S1, Supporting Information) that was performed for the specific layer stack used in this work shows that the expected change in J_{sc} is only on the order of 0.1 – 0.2 mA cm^{-2} for a perovskite layer of 150 nm that was estimated from the SEM cross-section. An over- or underestimation of the layer thickness or the absorption coefficient, which is within the experimental error, could increase this value up to 1.5 mA cm^{-2} , as also seen in Figure S1. An increased surface roughness for the ZnO-based devices, therefore, remains as the third, most likely option and will be discussed in more detail later.

Hereafter, we introduced a thickness-insensitive PDINO layer with a high conductivity of $7.6 \times 10^{-5} \text{ S cm}^{-1}$ ³⁶ as a replacement of the ZnO layer. The high conductivity of PDINO originates from its self-organized π -stacking in film, which allows overcoming the thickness limitation of commonly

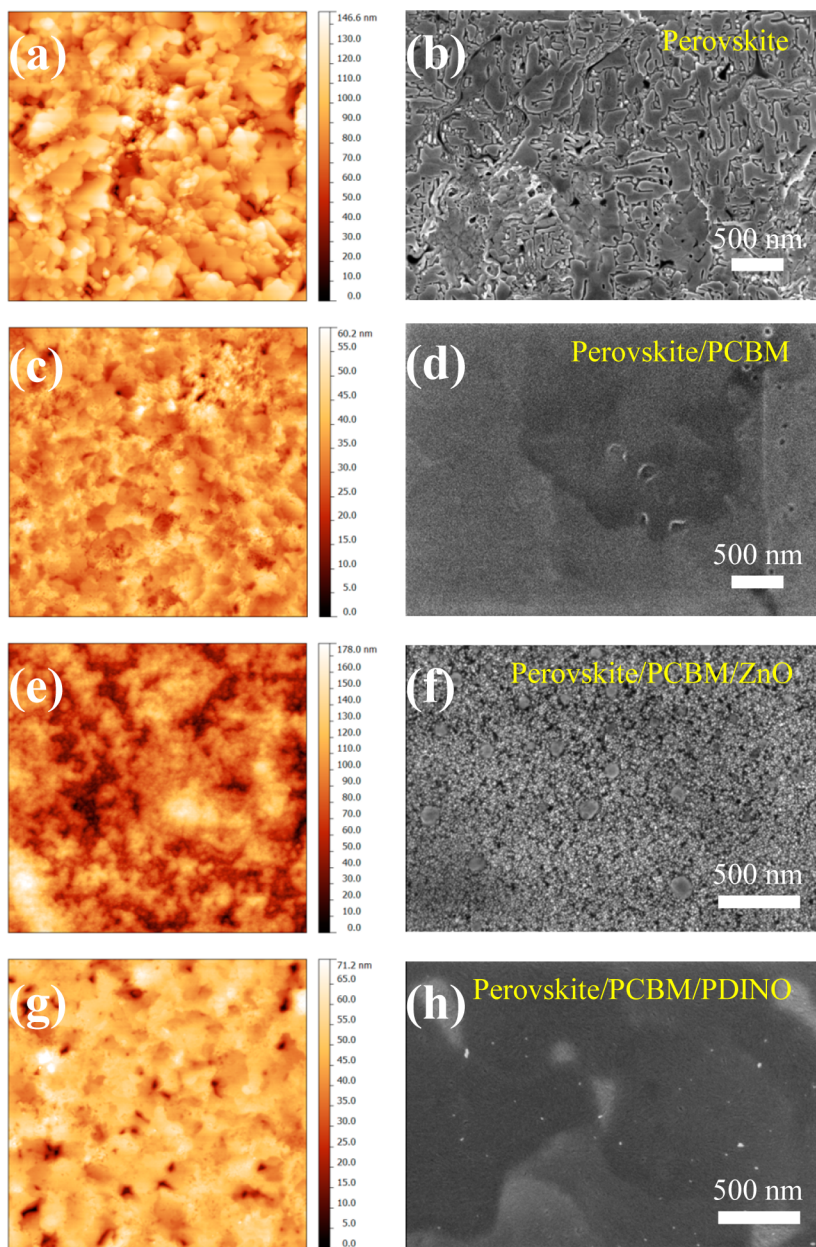


Figure 3. Surface topographic AFM images (size: $20 \times 20 \mu\text{m}$) of (a) the $\text{CH}_3\text{NH}_3\text{PbI}_{3-x}\text{Cl}_x$ perovskite layer on top of the PEDOT:PSS layer, (c) after deposition of PCBM on the PEDOT:PSS/perovskite composite layer, and after deposition of ZnO (e) or PDINO (g) on the PEDOT:PSS/perovskite/PCBM composite layer. SEM images of the related $\text{CH}_3\text{NH}_3\text{PbI}_{3-x}\text{Cl}_x$ perovskite films depicted in (a), (c), (e), and (g) are corresponding to (b), (d), (f), and (h), respectively.

used EELs (5–10 nm). To demonstrate this point, devices with various PDINO thicknesses have been investigated by varying the spin-coating speeds and the PDINO concentrations. The photovoltaic parameters of these devices with various PDINO thicknesses are shown in Figure S2 and Table S1 (see the Supporting Information). For PDINO-based devices, prominent PCEs over 13% are achieved within a wide range of the PDINO thicknesses (5–24 nm). These results directly illustrate that PDINO is a thickness-insensitive cathode interlayer used for perovskite solar cells, thus making it compatible with large area roll-to-roll processing. As shown in Figure 2c and Table 1, under AM 1.5G illumination, the optimized PCBM/PDINO/Ag device with a PDINO thickness of 15 nm does show an increase not only in J_{sc} (18.8 mA cm^{-2}) but also in V_{oc} (0.95 V) and FF (78.5%), leading to a high PCE of 14.0%. This is a

relative increase by 40% as compared to the control PCBM/Ag device (10.0%) and ca. 27% as compared to the PCBM/ZnO/Ag device (11.3%). Moreover, R_s is reduced from 10.62 to 0.83 $\Omega \text{ cm}^2$ and, most importantly, R_{sh} increases from 1.71 to 13.70 $\text{k}\Omega \text{ cm}^2$, as compared to the PCBM/Ag device. This directly enhances the FF values closing to 80%. In addition, compared to the PCBM/ZnO/Ag device, the lower R_s and increased R_{sh} of the PCBM/PDINO/Ag device suggest that Ag atoms are effectively prevented from diffusion through the PDINO layer and from directly contacting the perovskite semiconductor. Our previous work further showed that PDINO can decrease the work function of the Ag electrode, and can minimize the energy barrier between PCBM and the top Ag electrode, thus resulting in a lower contact resistance.³⁶ Correspondingly, the locally

higher, electrical field was also suggested to be beneficial to charge extraction and to reduce recombination losses.³⁸

Snaith et al. demonstrated that some perovskite solar cells showed photocurrent hysteresis at certain voltage scanning rates (or sweep delay time) and scan directions.³⁹ They also mentioned that this hysteresis may be due to either the charge traps of the low quality perovskite film, ferroelectric properties of perovskite material, and/or the electromigration of ions in the perovskite layers. Therefore, in this work, we also used different sweep delay times and two opposite scan directions to measure J - V curves, and the results are displayed in Figure S4 (Supporting Information). The performance of our high efficiency device did not show reduction when it was tested with various sweep delay times. In addition, Figure S2b presents the J - V curves for a device fabricated with the PDINO layer, measured with a 500 ms scanning delay in forward (from negative to positive bias) and reverse (from positive to negative bias) modes under AM 1.5 G illumination. It can be seen that no obvious photocurrent hysteresis was observed by changing the voltage sweep rates or scan directions. The slight difference in the J - V curves of the forward and reverse scans of the PCBM/PDINO/Ag device could be attributed to the normal decay of the cell measured in air. Thus, the device fabricated with our method and employed an effective PDINO interface layer has a negligible amount of charge traps and, therefore, has high device performance.

To verify the enhancement of J_{sc} , we performed EQE measurements of the devices with various cathodes in air, as shown in Figure 2d. All devices exhibited broad EQE curves throughout the visible to the near-IR regime (300–800 nm), consistent with the UV-vis absorption spectra. The J_{sc} values calculated from the EQE spectra are 16.46 mA cm⁻² for the PCBM/Ag device, 14.95 mA cm⁻² for the PCBM/ZnO/Ag device, and 17.55 mA cm⁻² for the PCBM/PDINO/Ag device, which are in good agreement with the values obtained from AM 1.5G measurements, again in air (Table 1). The slightly lower J_{sc} values obtained from the EQE measurements are caused either by device degradation during the measurements or by an underestimated spectral mismatch factor. The highest PCE (14.0%) of the PCBM/PDINO/Ag device is consistent with a high EQE value with the largest improvement in the 500–800 nm range. The PCBM/ZnO/Ag device in contrast showed a reduced EQE in the long wavelength regime (500–800 nm, as seen in Figure 2b). In summary, our experimental findings are in excellent agreement with the hypothesis that insertion of a thin PDINO layer between the PCBM/metal cathode overcomes the interface losses for p-i-n architecture pero-HSCs with high work function metals (such as Ag used here).

2.3. Film Morphology. As mentioned and discussed above, interface engineering is an essential task to optimize the performance of pero-HSCs. A good uniformity of the perovskite film, which tends to have voids between the crystals, and a homogeneous coverage by the interface material are prerequisites of interface engineering for pero-HSCs.^{5,20,35} Here, we performed atomic force microscopy (AFM) and scanning electron microscopy (SEM) measurements to investigate the coverage and morphology of perovskite films covered with various interface layers.

Figure 3a,c,e,g shows the surface morphologies obtained by AFM, as measured in air. The surface of $\text{CH}_3\text{NH}_3\text{PbI}_{3-x}\text{Cl}_x$ perovskite film shows a root-mean-square (rms) roughness of 16.0 nm (Figure 3a). Deposition of PCBM on the top of the perovskite layer reduces the roughness significantly (rms

roughness decreases to 5.5 nm, as shown in Figure 3c). Panels (e) and (g) in Figure 3 compare the surface morphologies of ZnO and PDINO films on top of the perovskite/PCBM composite layer, respectively. Deposition of ZnO on top of perovskite/PCBM results in a significantly increased roughness from 5.5 to 25.0 nm. As shown in Figure 3e, the ZnO nanoparticles tend to aggregate on top of the perovskite/PCBM composite and thus result in the formation of island-like micron scale features with a large surface roughness. In contrast, a PDINO layer on top of the perovskite/PCBM composite is only slightly rougher than the perovskite/PCBM composite itself (rms roughness is 7.4 nm, as shown in Figure 3g).

Figure 3b,d,f,h, exhibits SEM top-view images of the related $\text{CH}_3\text{NH}_3\text{PbI}_{3-x}\text{Cl}_x$ perovskite composite films. As shown in Figure 3b, the pristine $\text{CH}_3\text{NH}_3\text{PbI}_{3-x}\text{Cl}_x$ perovskite film exhibits densely interconnected crystalline areas with length scales in the order of several hundred nanometers, which is consistent with the AFM topography image (Figure 3a). The perovskite film shows interconnected crystalline domains with visible voids. As shown in Figure 3d, PCBM almost completely covers the perovskite film with relatively smaller and fewer voids. As expected, SEM confirms that ZnO on top of a perovskite/PCBM composite indeed increases the surface roughness significantly (Figure 3f). As already discussed above, such an enhanced surface roughness may adversely affect the quality of the top metal cathode and reduce the device performance. Figure 3h shows the SEM top-view image of a perovskite/PCBM/PDINO composite, stating that PDINO indeed gives a homogeneous and high qualitative coverage of the perovskite/PCBM stack.

2.4. Device Stabilities. With these impressive device efficiencies, the device stabilities were also investigated for perovskite solar cells with various cathodes. Figure 4 shows the

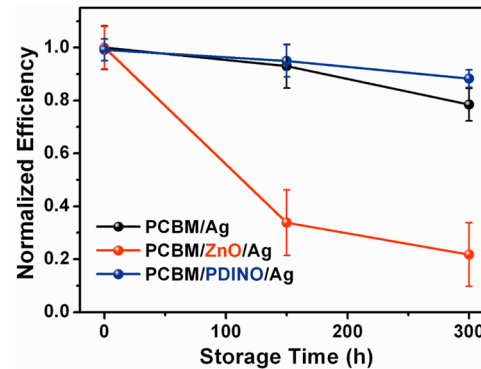


Figure 4. Normalized cell efficiency plotted as a function of storage time for perovskite solar cells with PCBM/Ag, PCBM/ZnO/Ag, and PCBM/PDINO/Ag cathodes stored in air. Measurements were made on six devices of each type without any encapsulation, and the error bars represent plus or minus 1 standard deviation from the mean.

normalized efficiency versus storage time for the relevant devices with PCBM/Ag, PCBM/ZnO/Ag, and PCBM/PDINO/Ag cathodes, without any encapsulation. Here, we first investigated the loss in device performance when the devices with PCBM/Ag, PCBM/ZnO/Ag, and PCBM/PDINO/Ag cathodes were stored under ambient conditions (relative humidity ca. 5%; temperature ca. 22 °C). Though they were stored in the same conditions, the average degradation rate of the device with the PCBM/ZnO/Ag cathode was

significantly faster than these PCBM/PDINO/Ag-based devices. As can be seen in Figure 4, the efficiencies of PCBM/PDINO/Ag devices maintained at ca. 90% of their initial values after 300 h. Notably, the better device stability of the PCBM/PDINO/Ag devices over the control PCBM/Ag devices is probably related to the self-encapsulation effect of the PDINO layer acting as a protective barrier. These results illustrate that the PDINO layer is a promising interface layer for achieving air-stable high-performance pero-HSCs, while the ease of manufacturing via printing processes is maintained.

3. CONCLUSIONS

In summary, we successfully fabricated efficient p-i-n $\text{CH}_3\text{NH}_3\text{PbI}_{3-x}\text{Cl}_x$ pero-HSCs using a metal oxide (ZnO) and an *n*-type small molecule (PDINO) as EELs. Both, ZnO and PDINO layers can effectively modify the PCBM/Ag interface and increase the V_{oc} values (from 0.85 to 0.95 V). Although the PCBM/ ZnO /Ag device shows an improved PCE of 11.3% as compared to the control PCBM/Ag device (10.0%), its J_{sc} value is slightly reduced, either due to optical effects or, most likely, due to a reduced current collection from the rougher interface or due to a combination of both mechanisms. Hereafter, the PCE was further improved to 14.0% under AM 1.5G illumination by inserting a well conducting n-type PDINO layer between PCBM and the Ag electrode. Notably, PDINO-based devices showed prominent PCEs over 13% within a wide range of the PDINO thicknesses (5–24 nm). PDINO offers, on the one hand, the desired electronic levels for electron extraction, gives homogeneous and smooth films with a good collection probability, and low R_s , and, on the other hand, successfully prevents the diffusion of Ag ions to the semiconductor interface. Besides the device performance results, PDINO-based devices also show the higher device stability as opposed to these of devices with PCBM/Ag and PCBM/ ZnO /Ag cathodes. The ability to obtain high efficiency and stability using PDINO expands the present, rather limited, range of available cathode interface layers for pero-HSCs. We expect that this study opens a smart strategy for developing high-performance and long-time stable pero-HSCs on rigid as well as flexible substrates or mass production compatible with coating techniques.

■ ASSOCIATED CONTENT

S Supporting Information

Experimental section, the optical calculated short-circuit current of devices with various perovskite layer thicknesses as a function of the ZnO layer thickness (Figure S1), the PDINO thickness dependency on photovoltaic performance (Figure S2 and Table S1), histograms of device parameters (Figure S3), $J-V$ curves measured with different delay times or with different sweep directions (Figure S4), and normalized cell efficiency of the PCBM/PDINO/Ag device plotted as a function of storage time stored in a glovebox without and with 50 °C (Figure S5). This material is available free of charge via the Internet at <http://pubs.acs.org>.

■ AUTHOR INFORMATION

Corresponding Authors

*E-mail: zgzhangwhu@iccas.ac.cn (Z.-G.Z.).

*E-mail: Hamed.Azimi@ww.uni-erlangen.de (H.A.).

Notes

The authors declare no competing financial interest.

■ ACKNOWLEDGMENTS

The authors gratefully acknowledge the support of the Cluster of Excellence “Engineering of Advanced Materials” at the University of Erlangen-Nuremberg, which is funded by the German Research Foundation (DFG) within the framework of its “Excellence Initiative”. This organic molecule oriented part of the work was supported by the Sonderforschungsbereich 953 “Synthetic Carbon Allotropes” as well as the China Scholarship Council (CSC). Z.-G.Z. and Y.L. thank the National Program on Key Basic Research Project (973 Program, 2014CB643501) (China) and the Strategic Priority Research Program of the Chinese Academy of Sciences (no. XDB12030200) for financial support. T.P. acknowledges funding via the DFG research training group GRK 1896. C.B. acknowledges the support of the EU-project SOLPROCEL (“SOLUTION PROCESSED HIGH PERFORMANCE TRANSPARENT ORGANIC PHOTOVOLTAIC CELLS”, Grant no. 604506). K.F. acknowledges use of the services and facilities of the Energie Campus Nürnberg and financial support through the “Aufbruch Bayern” initiative of the state of Bavaria. We also acknowledge support from the Bavarian Initiative “Solar Technologies go Hybrid” (SolTech project) and from the Bavarian Initiative “Solarfactory of the future” within the Energy Campus Nürnberg (EnCN).

■ REFERENCES

- (1) Kojima, A.; Teshima, K.; Shirai, Y.; Miyasaka, T. *J. Am. Chem. Soc.* **2009**, *131*, 6050.
- (2) Im, J. H.; Lee, C. R.; Lee, J. W.; Park, S. W.; Park, N. G. *Nanoscale* **2011**, *3*, 4088.
- (3) Lee, M. M.; Teuscher, J.; Miyasaka, T.; Murakami, T. N.; Snaith, H. J. *Science* **2012**, *338*, 643.
- (4) Heo, J. H.; Im, S. H.; Noh, J. H.; Mandal, T. N.; Lim, C. S.; Chang, J. A.; Lee, Y. H.; Kim, H. J.; Sarkar, A.; Nazeeruddin, M. K.; Gratzel, M.; Seok, S. I. *Nat. Photonics* **2013**, *7*, 486.
- (5) Liu, M.; Johnston, M. B.; Snaith, H. J. *Nature* **2013**, *501*, 395.
- (6) Mitzi, D. B. *Chem. Mater.* **1996**, *8*, 791.
- (7) Koh, T. M.; Fu, K.; Fang, Y.; Chen, S.; Sum, T. C.; Mathews, N.; Mhaisalkar, S. G.; Boix, P. P.; Baikie, T. *J. Phys. Chem. C* **2014**, *118*, 16458.
- (8) Kagan, C. R.; Mitzi, D. B.; Dimitrakopoulos, C. D. *Science* **1999**, *286*, 945.
- (9) Etgar, L.; Gao, P.; Xue, Z.; Peng, Q.; Chandiran, A. K.; Liu, B.; Nazeeruddin, M. K.; Graetzel, M. *J. Am. Chem. Soc.* **2012**, *134*, 17396.
- (10) Chen, Q.; Zhou, H.; Zirou, H.; Lou, S.; Duan, H.; Wang, H.; Liu, Y.; Li, G.; Yang, Y. *J. Am. Chem. Soc.* **2014**, *136*, 622.
- (11) Burschka, J.; Pellet, N.; Moon, S. J.; Humphry-Baker, R.; Gao, P.; Nazeeruddin, M. K.; Gratzel, M. *Nature* **2013**, *499*, 316.
- (12) (a) Park, N. G. *J. Phys. Chem. Lett.* **2013**, *4*, 2423. (b) Service, R. F. *Science* **2014**, *344*, 458.
- (13) Xing, G.; Mathews, N.; Sun, S.; Lim, S. S.; Lam, Y. M.; Gratzel, M.; Mhaisalkar, S.; Sum, T. C. *Science* **2013**, *342*, 344.
- (14) Eperon, G. E.; Burlakov, V. M.; Docampo, P.; Goriely, A.; Snaith, H. J. *Adv. Funct. Mater.* **2014**, *24*, 151.
- (15) (a) Liang, P. W.; Liao, C. Y.; Chueh, C. C.; Zuo, F.; Williams, S. T.; Xin, X. K.; Lin, J. J.; Jen, A. K.-Y. *Adv. Mater.* **2014**, *26*, 3748. (b) Xue, Q.; Hu, Z.; Liu, J.; Lin, J.; Sun, C.; Chen, Z.; Duan, C.; Wang, J.; Liao, C.; Lau, W. M.; Huang, F.; Yip, H.-L.; Cao, Y. *J. Mater. Chem. A* **2014**, *2*, 19598.
- (16) (a) Docampo, P.; Ball, J. M.; Darwich, M.; Eperon, G. E.; Snaith, H. J. *Nat. Commun.* **2013**, *4*, 2761. (b) Malinkiewicz, O.; Yella, A.; Lee, Y. H.; Espallargas, G. M.; Graetzel, M.; Nazeeruddin, M. K.; Bolink, H. J. *Nat. Photonics* **2014**, *8*, 128.
- (17) (a) Wang, Q.; Shao, Y. C.; Dong, Q. F.; Xiao, Z. G.; Yuan, Y. B.; Huang, J. S. *Energy Environ. Sci.* **2014**, *7*, 2359. (b) Xiao, Z. G.; Bi, C.; Shao, Y. C.; Dong, Q. F.; Wang, Q.; Yuan, Y. B.; Wang, C. G.; Gao, Y. L.; Huang, J. S. *Energy Environ. Sci.* **2014**, *7*, 2619.

- (18) Conings, B.; Baeten, L.; Dobbelaere, C. D.; D'Haen, J.; Manca, J.; Boyen, H. G. *Adv. Mater.* **2014**, *26*, 2041.
- (19) Sun, S.; Salim, T.; Mathews, N.; Duchamp, M.; Boothroyd, C.; Xing, G.; Sum, T. C.; Lam, Y. M. *Energy Environ. Sci.* **2014**, *7*, 399.
- (20) Green, M. A.; Ho-Baillie, A.; Snaith, H. J. *Nat. Photonics* **2014**, *8*, 506.
- (21) Kwon, Y. S.; Lim, J.; Yun, H.-J.; Kim, Y.-H.; Park, T. *Energy Environ. Sci.* **2014**, *7*, 1454–1460.
- (22) Zhou, H.; Chen, Q.; Li, G.; Luo, S.; Song, T. B.; Duan, H. S.; Hong, Z.; You, J.; Liu, Y.; Yang, Y. *Science* **2014**, *345*, 542.
- (23) Jeon, N. J.; Lee, H. G.; Kim, Y. C.; Seo, J.; Noh, J. H.; Lee, J.; Seok, S. I. *J. Am. Chem. Soc.* **2014**, *136*, 7837.
- (24) Ryu, S.; Noh, J. H.; Jeon, N. J.; Chan Kim, Y.; Yang, W. S.; Seo, J.; Seok, S. I. *Energy Environ. Sci.* **2014**, *7*, 2614.
- (25) You, J. B.; Hong, Z. R.; Yang, Y.; Chen, Q.; Cai, M.; Song, T. B.; Chen, C. C.; Lu, S. R.; Liu, Y. S.; Zhou, H. P.; Yang, Y. *ACS Nano* **2014**, *8*, 1674.
- (26) Seo, J. H.; Gutacker, A.; Sun, Y. M.; Wu, H. B.; Huang, F.; Cao, Y.; Scherf, U.; Heeger, A. J.; Bazan, G. C. *J. Am. Chem. Soc.* **2011**, *133*, 8416.
- (27) Khan, T. M.; Zhou, Y. H.; Dindar, A.; Shim, J. W.; Fuentes-Hernandez, C.; Kippelen, B. *ACS Appl. Mater. Interfaces* **2014**, *6*, 6202.
- (28) Min, J.; Luponosov, Y. N.; Zhang, Z.-G.; Ponomarenko, S. A.; Ameri, T.; Li, Y. F.; Brabec, C. J. *Adv. Energy Mater.* **2014**, *4*, 1400816.
- (29) Seo, J. W.; Park, S.; Kim, Y. C.; Jeon, N. J.; Noh, J. H.; Yoon, S. C.; Seok, S. I. *Energy Environ. Sci.* **2014**, *7*, 2624.
- (30) Chiang, C.-H.; Tseng, Z.-L.; Wu, C.-G. *J. Mater. Chem. A* **2014**, *2*, 15897.
- (31) Kim, H.-B.; Choi, H.; Jeong, J.; Kim, S.; Walker, B.; Song, S.; Kim, J. Y. *Nanoscale* **2014**, *6*, 6679.
- (32) Min, J.; Luponosov, Y. N.; Gerl, A.; Polinskaya, M. S.; Peregudova, S. M.; Dmitryakov, P. V.; Bakirov, A. V.; Shcherbina, M. A.; Chvalun, S. N.; Grigorian, S.; K-Busies, N.; Ponomarenko, S. A.; Ameri, T.; Brabec, C. J. *Adv. Energy Mater.* **2014**, *4*, 1301234.
- (33) Min, J.; Zhang, Z.-G.; Zhang, S. Y.; Li, Y. F. *Chem. Mater.* **2013**, *5*, 5609.
- (34) Stranks, S. D.; Eperon, G. E.; Grancini, G.; Menelaou, C.; Alcocer, M. J. P.; Leijtens, T.; Herz, L. M.; Petrozza, A.; Snaith, H. J. *Science* **2013**, *342*, 341.
- (35) Wang, K. C.; Jeng, J. Y.; Shen, P. S.; Chang, Y. C.; Diau, E. W. G.; Tsai, C. H.; Chao, T. Y.; Hsu, H. C.; Lin, P. Y.; Chen, P.; Guo, T. F.; Wen, T. C. *Sci. Rep.* **2014**, *4*, 4756.
- (36) Zhang, Z. G.; Qi, B. Y.; Jin, Z. W.; Chi, D.; Qi, Z.; Li, Y. F.; Wang, J. Z. *Energy Environ. Sci.* **2014**, *7*, 1966.
- (37) (a) Stubhan, T.; Ameri, T.; Salinas, M.; Krantz, J.; Machui, F.; Halik, M.; Brabec, C. J. *Appl. Phys. Lett.* **2011**, *98*, 253308. (b) Stubhan, T.; Li, N.; Luechinger, N. A.; Halim, S. C.; Matt, G. J.; Brabec, C. J. *Adv. Energy Mater.* **2012**, *2*, 1433. (c) Ameri, T.; Dennler, G.; Waldauf, C.; Azimi, H.; Seemann, A.; Forberich, K.; Hauch, J.; Scharber, M.; Hingerl, K.; Brabec, C. J. *Adv. Funct. Mater.* **2010**, *20*, 1592. (d) Kim, J. Y.; Kim, S. H.; Lee, H.-H.; Lee, K.; Ma, W. L.; Gong, X.; Heeger, A. J. *Adv. Mater.* **2006**, *18*, 572.
- (38) Kyaw, A. K. K.; Wang, D. H.; Gupta, V.; Leong, W. L.; Ke, L.; Bazan, G. C.; Heeger, A. J. *ACS Nano* **2013**, *7*, 4569.
- (39) Snaith, H. J.; Abate, A.; Ball, J. M.; Eperon, G. E.; Leijtens, T.; Noel, N. K.; Stranks, S. D.; Wang, J. T.-W.; Wojciechowski, K.; Zhang, W. J. *Phys. Chem. Lett.* **2014**, *5*, 1511.